Biosensors and Bioelectronics 268 (2025) 116885

Contents lists available at ScienceDirect

Biosensors and Bioelectronics

journal homepage: www.elsevier.com/locate/bios

Silver shelled gold nanorods for sensitive detection of cholesterol and triglycerides

Mitali Basak [a], Harshal B. Nemade [a,c,d], Dipankar Bandyopadhyay [a,b,c,*]

[a] Centre for Nanotechnology, Indian Institute of Technology Guwahati, Assam, 781039, India
[b] Department of Chemical Engineering, Indian Institute of Technology Guwahati, Assam, 781039, India
[c] Jyoti and Bhupat Mehta School of Health Sciences and Technology, Indian Institute of Technology Guwahati, Assam, 781039, India
[d] Department of Electronics and Electrical Engineering, Indian Institute of Technology Guwahati, Assam, 781039, India

ARTICLE INFO

Keywords:
Silver shelled gold nanorods
LSPR
Cholesterol
Triglycerides biosensor
SERS

ABSTRACT

We report the synthesis of bimetallic plasmonic nanostructure of silver shelled gold nanorods (Ag–Au NRs), subsequently employed for the selective detection of cholesterol (Cho) and triglycerides (TGl) utilizing Surface Enhanced Raman Spectroscopy (SERS). In this direction, the gold nanorods (Au NRs) were synthesized via seed mediated growth method followed by forming a silver shell with reduction of $AgNO_3$ onto Au NRs. Ag–Au NRs showed significantly augmented SERS property owing to hybridization of Localized Surface Plasmon Resonances (LSPR) of silver and gold. The enhanced plasmonic property was thus employed for biosensing. For this, two different Raman reporter molecules, 5,5′–dithiobis–(2–nitrobenzoic acid) (DTNB) and 4–aminothiophenol (4ATP) were immobilized separately on Ag–Au NRs to synthesize SERS active nanoprobes, before the attachment of the bioreceptors – cholesterol oxidase (ChOx) and lipase (Lp) to form ChOx–DTNB–Ag–Au NRs and Lp–4ATP–Ag–Au NRs. These nanoprobes were then utilized for the quantification of Cho and TGl via liquid mode Raman spectroscopic study. The change in SERS spectral intensity of DTNB and 4ATP were systematically recorded in reference to the baseline sample to mark the calibration for both Cho and TGl. Additionally, interference studies considering effects of ascorbic acid, glucose, sodium and potassium ion were performed to unveil excellent selectivity of the proposed method.

1. Introduction

The fat components of healthy human diets play a pivotal role in the synthesis of a range of essential biomaterials inside the body that include vitamins, hormones, steroids, among others (Anderson and Williams, 1937). They are also the building blocks of cell membrane and various cell organelles, responsible for transporting fat–soluble vitamins A, D, E, K through the bloodstream (Morris and Mohiuddin, 2020), participate in the storage of energy before 'burning' to revive a human body and produce fatty acid, a pivotal element for human survival (Johnson and Mohn, 2015; Mellanby, 1933). A healthy fat metabolism maintains adequate levels of cholesterol and triglycerides in the blood, ensuring optimal physiological function of the body (Kritchevsky, 1995; Lawrence, 2010). However, excess or inadequate amount of these in the blood serum are indicators of the onset of various metabolic and cardiovascular disorders (Wakil and Abu-Elheiga, 2009). On the other hand, the modern medicine depend heavily on the blood cholesterol and triglycerides in assessing and managing cardiovascular health (Soppert et al., 2020) because the plaque tends to clog the arteries to engender various cardiovascular complications in the human body. It is now well understood that the routine measurement of cholesterols and triglycerides at the patient's site employing a point–of–care–testing (POCT) device can help in the early detection of diverse cardiovascular complications at the early stage.

Predominantly, Cho is synthesized in the liver via *de novo* synthesis. Being insoluble in water, the bipolar biomolecules such as high density lipoproteins (HDL) and low density lipoproteins (LDL) transport cholesterol throughout the body (Trajkovska and Topuzovska, 2017). The LDL carries cholesterol from liver to the cells for utilization in various metabolic functions. The cells release the surplus cholesterol into the bloodstream which is reclaimed by HDL and transport to liver for elimination. Therefore, any imbalance between the LDL and HDL elevate the cholesterol accumulation in the blood causing plaque formation in the arterial walls (Norum et al., 1983). If left untreated, it can

* Corresponding author. Department of Chemical Engineering, Indian Institute of Technology Guwahati, Assam, 781039, India.
E-mail address: dipban@iitg.ac.in (D. Bandyopadhyay).

https://doi.org/10.1016/j.bios.2024.116885
Received 5 July 2024; Received in revised form 26 September 2024; Accepted 27 October 2024
Available online 28 October 2024

cause adverse cardiovascular diseases like hypertension, reduced blood flow, formation of blood clots, ischemia, peripheral artery disease and among others (Lawes et al., 2004). On the other hand, TGl are primarily consumed via dietary intake. Once ingested, these are converted into fatty acids and glycerol during digestion, which in turn is absorbed in the bloodstream and packaged inside lipoproteins, especially very low-density lipoprotein (VLDL) for transportation to the cells. The excess and unutilized TGl are stored in the adipose tissues for future use. An elevated level of TGl level leads to hypertriglyceridemia causing various fatalities like atherosclerosis and coronary artery disease, pancreatitis, metabolic syndrome, type 2 diabetes, fatty liver and among others (Nordestgaard and Varbo, 2014). Therefore, the timely detection of any abnormality and monitoring of cholesterol and triglyceride levels in the blood is highly sought for.

Conventionally, Blood Lipid Profile testing is the gold standard for the identification of Cho and TG levels in the blood (Nordestgaard, 2017). According to National Lipid Association and the National Cholesterol Education Program (NCEP), the prescribed cholesterol level in blood is < 200 mg/dL for adults and <170 mg/dL for children (Children and Pediatrics, 1992). For TGl, the recommended level is < 150 mg/dL for adults and <90 mg/dL for children (Stein and Myers, 1995). Although the blood profile test is widely accepted, various technological advancements have emerged to improve the efficiency and efficacy of the examination and contribute to a more patient–friendly diagnostic approach. Considering this, numerous researches have been made for enzymatic detection of Cho and TGl viz, electrochemical sensors (Amiri and Arshi, 2020) employing voltammetric/amperometry detection techniques utilizing carbonaceous materials (Mondal et al., 2017) or nanostructures (Mitra and Basak, 2022), colorimetric and plasmonic sensing using plasmonic nanostructures (Basak et al. 2021a, 2022; Basak et al., 2022), chemiresistive sensors (Yang et al., 2023), semiconductor devices biosensors (Hooda et al., 2018), and among others. Therefore, the new innovations for advancing the blood lipid test and making it less invasive by incorporating cutting–edge approaches that can surpass current standards and is fervently pursued.

SERS is a pioneering, non–destructive and state–of–art analytical technique that has been widely accepted for transformative approach to molecular characterization (Tahir et al., 2021). The localization of electric field in the vicinity of the plasmonic metal nanostructures owing to the LSPR characteristic, creates “hotspots” of electron density surrounding the metal nanostructures (Haes et al., 2004). These hotspots serve as the source for intense spectral recognition in SERS, thus surpassing the limitations of Raman Spectroscopy (Zhang et al., 2017). It has revolutionized the nanoscale light–matter interaction based biosensing approaches surpassing diffraction limits and enhancing the near field intensity (Giannini et al., 2010). Several studies have been reported for designing the highly SERS active metal nanostructures targeting label free, single cell/molecule detection for precise and novel biosensing purposes (Sun et al., 2019).

In view of the above background, the present work focuses on the development of a SERS based multiplexing principle for the concurrent detection of Cho and TGl. For this purpose, the SERS active bimetallic nanostructures, Ag–Au NRs, were synthesized chemically. The plasmonic resonance hybridization of silver and gold produces significantly augmented spectral resolutions as compared to pristine silver or gold nanorods. Subsequently, the Ag–Au NRs were linked to two different Raman active receptors and immobilized with ChOx and Lp for concurrent detection of different concentrations of Cho and TGl. SERS examinations and the selectivity test with different interfering agents proved the efficiency of the proposed methodology for steadfast biosensing applications.

2. Materials and methods

2.1. Materials

All reagents and related instruments are listed in section S1 of the Electronic Supporting Information (ESI).

2.2. Methods

All experimental methods are mentioned in section S1 of the ESI.

3. Results and discussion

3.1. Characterization of Au NRs

Here, the Au NRs was synthesized via seed mediated growth method, as described in the ESI. Fig. 1 shows the morphological characterizations of the synthesized Au NRs. The UV–Vis spectroscopic spectrum in Fig. 1 (a) shows two characteristic LSPR peaks – transverse peak at ~ 518 nm and longitudinal peak at ~ 645 nm which confirms the formation of the anisotropic nanostructure. Besides, Fig. 1(b) shows the Field Emission Transmission Electron Microscopy (FETEM) and the High–Resolution Transmission Emission Microscopy (HRTEM) (Fig. 1(b)inset) imaging of the Au NRs confirming the formation of rod-like structure with (i) diameter of ~14 nm and (ii) length of ~32 nm. The ring appearance of the diffraction pattern (DP) recorded in Selected Area Electron Diffraction (SAED) pattern in Fig. 1(c) shows the merger of the field of many single crystals of the single crystalline Au NRs. The Au NRs was further utilized for the synthesis of Ag-Au NRs by chemical reduction of $AgNO_3$ on the surface of Au NRs to form the silver shell over the Au NRs.

3.2. Characterization of Ag–Au NRs

Fig. 2 depicts the morphological characterizations of the as-synthesized Ag-Au NRs. The UV–Vis characterization in Fig. 2(a) shows a significant shift of the spectrum of Au NRs to ~ 415 nm after the chemical synthesis of Ag-Au NRs. This spectral shift confirms the formation of Ag shell over the Au NRs as the characteristic LSPR spectrum of Ag lies within this specific domain (Zhu et al., 2018). The broadening of UV–Vis spectrum of the Ag-Au NRs could be attributed to (i) the LSPR spectral coupling of both Au and Ag, and (ii) the polydispersity of the synthesized Ag-Au NRs as shown in the FETEM images. Also, the stronger plasmonic response of Ag than Au resulted in remarkably intense absorbance in Ag-Au NRs as compared to Au NRs.

Moreover, the FETEM and HRTEM images (inset) in Fig. 2(b)(i), 2(b)(iii), and 2(b)(iv) depict the morphology of Ag–Au NRs indicating the formation of a complete envelope over the Au NRs. To verify the composition of the envelope over the Au NRs, elemental mapping was performed in FETEM. Fig. 2(b)(ii) shows the elemental mapping of Fig. 2(b)(i) illustrating the presence of Ag and Au over the entire mapped area. These images confirm the formation of fully-grown Ag shell enveloping the Au NRs. The diffused grains with circular DP appeared in SAED pattern in Fig. 2(c) depicts the recording of the DP in the field of many single crystals of the Ag–Au NRs.

3.3. Preparation of DTNB–Ag–Au NRs and 4ATP–Ag–Au NRs SERS nanoprobes

Subsequently, the Ag-Au NRs was modified to prepare SERS nanoprobes for the biosensing application. For this purpose, two Raman reporter molecules – DTNB and 4ATP were immobilized distinctly on Ag–Au NRs via gold thiol coordination bonding. The preparation steps for DTNB–Ag–Au NRs and 4ATP–Ag–Au NRs SERS nanoprobes are given in ESI. The immobilization of DTNB or 4ATP on Ag–Au NRs were confirmed using Raman Spectroscopic characterization in liquid mode which shows the appearance of characteristic molecular vibrational

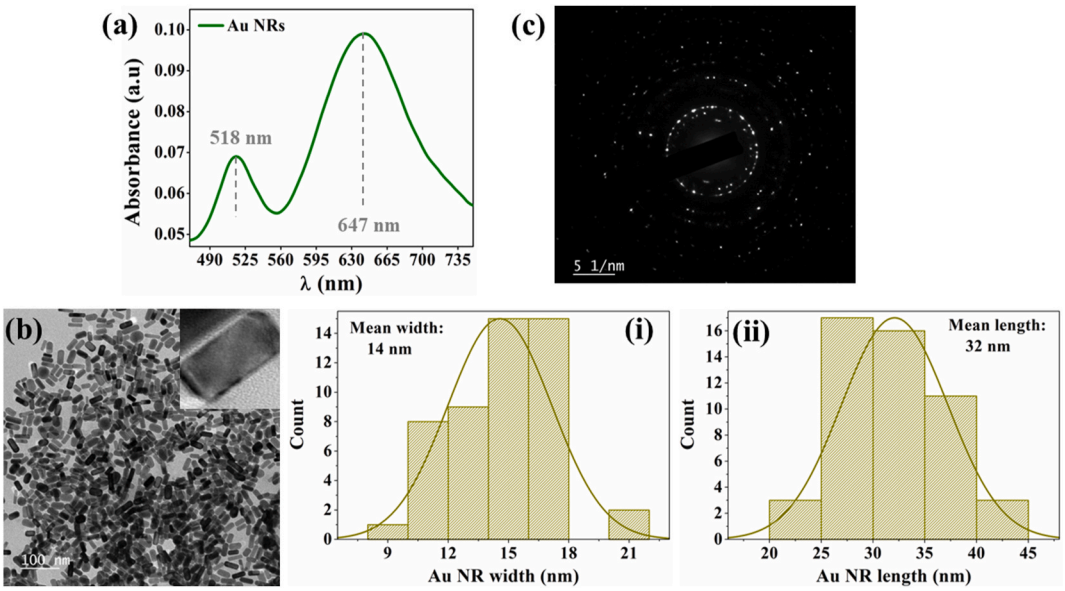

Fig. 1. Shows (a) UV–Vis spectrum of the synthesized Au NRs, (b) FETEM imaging of the Au NRs showing average diameter of ~14 nm (i) and length ~32 nm (ii), and (c) SAED pattern of the synthesized Au NRs.

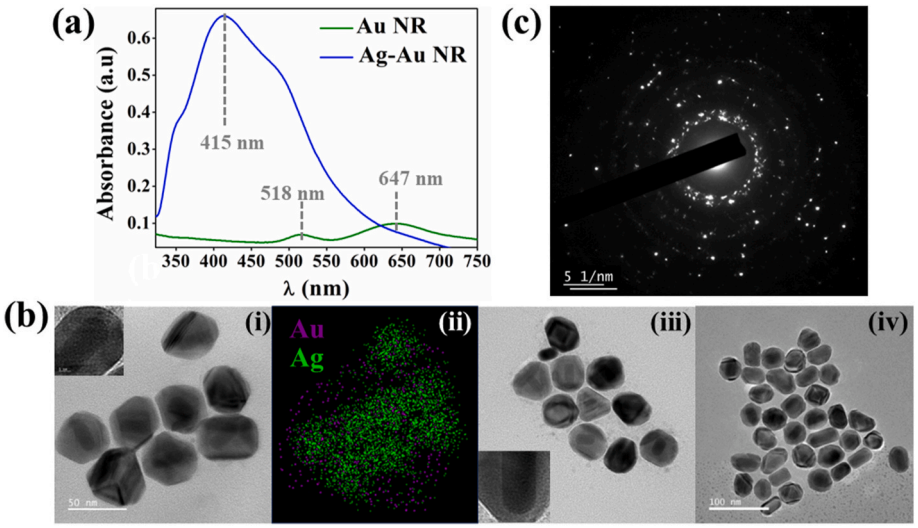

Fig. 2. Shows (a) UV–Vis spectrum of the Ag–Au NRs as compared to Au NRs, (b) (i), (iii) and (iv) FETEM images of the synthesized Ag–Au NRs, inset shows the HRTEM images depicting formation of the shell over Au NRs, (b)(ii) the elemental mapping of Ag and Au of (b)(i), and (c) SAED pattern of the synthesized Ag–Au NRs.

peaks of DTNB(Rhee et al., 2023) and 4ATP (Gabudean et al., 2011) on Ag–Au NRs, as shown in Fig. 3(a). The characteristic Raman bands of DTNB–Ag–Au NRs and 4ATP–Ag–Au NRs are listed in Table 1.

The Raman active molecules like DTNB or 4ATP are highly employed in SERS based biosensing applications owing to its significantly improved SERS spectral properties on immobilization to metallic nanostructures. The spectral enhancement ensures a high signal-to-noise ratio, even at low analyte concentrations, thereby providing competent sensing resolution.

3.4. *Characterization of plasmonic property*

The plasmonic spectral coupling of Ag and Au in Ag-Au NRs provides an enhanced LSPR characteristics as observed in Fig. 2(a). To validate the enhanced LSPR property of the Ag–Au NRs compared to Au NRs, plasmonic enhancement factor was examined using SERS characterization, as shown in Fig. 3(b). Fig. 3(b)(i) and 3(b)(ii) show the spectral enhancement observed in the Raman bands of DTNB and 4ATP, respectively, after immobilizing on both Ag–Au NRs and Au NRs. It could be inferred from the figure that the apex spectral peak of DTNB at 1333 cm^{-1} and 4ATP at 1077 cm^{-1} show ~20 fold and ~50 fold augmentation, respectively, when immobilized on Ag–Au NRs compared to Au NRs. Earlier studies report that the combination of plasmonic metal nanostructures like Ag and Au in Ag-Au NRs show strong enrichment of electric field around the nanostructures owing to synergistic hybridization of the plasmonic bands of the two metals (Jia et al., 2014), compared to Ag or Au independently. Therefore, one can infer that the remarkable plasmonic characteristics of Ag–Au NRs could be employed for sensitive detection of various biomolecules. A comparative examination of SERS spectral enhancement of DTNB and 4ATP on Au NRs and Ag-Au NRs, individually, is given in section S2 of the ESI for better comprehension.

The plasmonic enhancement of the synthesized Au NRs and Ag–Au NRs were also numerically simulated using COMSOL Multiphysics™

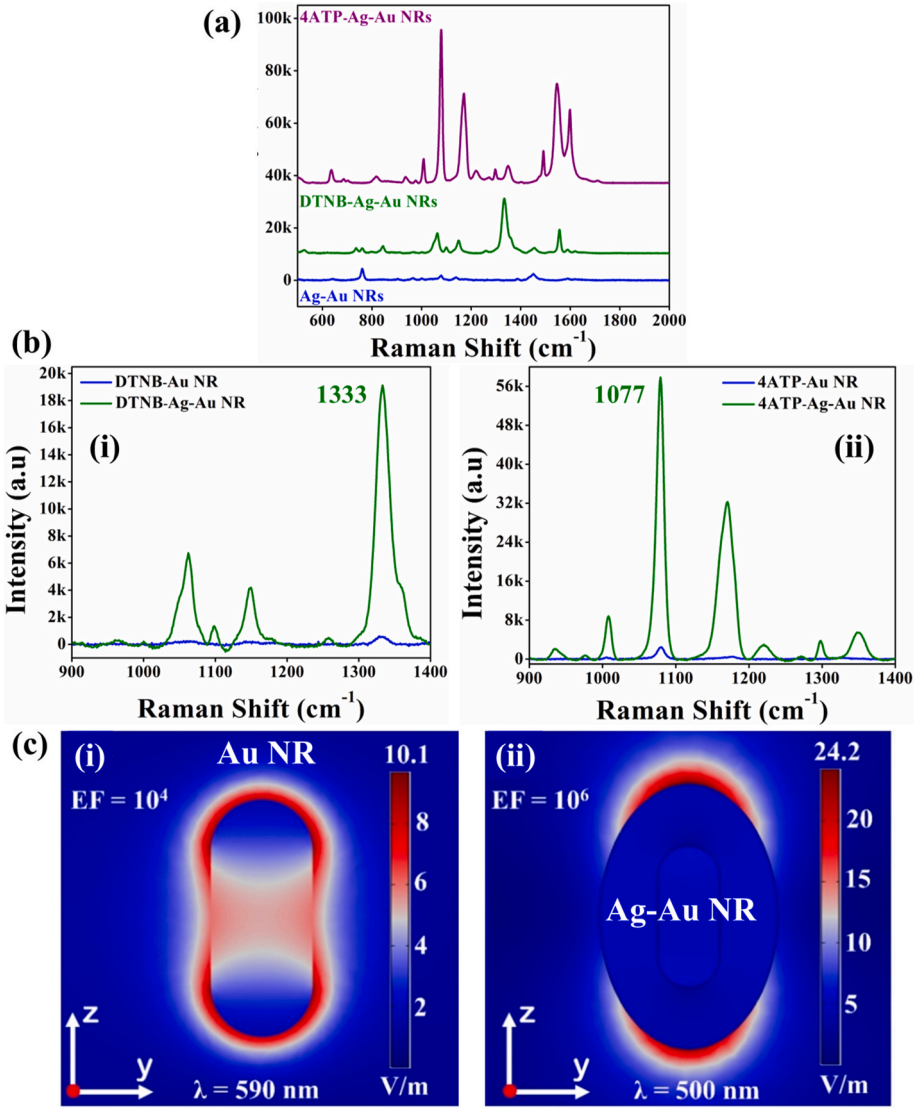

Fig. 3. Shows (a) characteristic Raman spectroscopic bands of DTNB–Ag–Au NRs and 4ATP–Ag–Au NRs as compared to pristine Ag–Au NRs, (b) the enhancement in SERS spectral peaks of (i) DTNB–Ag–Au NRs and (ii) 4ATP–Ag–Au NRs, and (c) simulation result for near field enhancement of (i) Au NR and (ii) Ag–Au NR.

Table 1
Characteristic Raman bands of DTNB and 4ATP.

DTNB–Ag–Au NRs		4ATP–Ag–Au NRs	
Raman band (cm^{-1})	**Assignment**	**Raman band (cm^{-1})**	**Assignment**
847	Scissoring vibration of NO_2 group	**1009**	C–C ring deformation
1063	Succinimidyl N–C–O stretching overlapped with aromatic ring modes	**1077**	C–C, C–S stretching
		1178	C–H bending
1152	C–H deformation modes	**1350**	C–N stretching
1333	Symmetric NO_2 group	**1492, 1545**	C–H bending and C–C vibration
1558	C–C stretching on aromatic ring	**1598**	NH_2 bending

based numerical simulation. The details of the simulation framework are discussed in section S3 of the ESI. Fig. 3(c)(i) and (ii) show the near field enhancement in an isolated Au NR showing theoretical enhancement factor, EF_t in the order of $\sim 10^4$ whereas for Ag–Au NR it is $\sim 10^6$. The simulation results demonstrate the EF_t of the Ag–Au NR is much higher as compared to Au NR as also obtained in the SERS characterization. Therefore, further experiments were carried out utilizing Ag–Au NRs for the biosensing application owing to its significantly enhanced plasmonic properties.

3.5. Biosensing of Cho and TG

For the concurrent detection of Cho and TGl, DTNB–Ag–Au NRs was immobilized with ChOx and 4ATP–Ag–Au NRs was immobilized with Lp utilizing EDC–NHS bioconjugation chemistry. The detailed enzyme immobilization procedure is discussed in ESI and shown schematically in Fig. 4(a). Fig. 4(b) (i) shows the UV–Vis characterization for the immobilization of DTNB and ChOx on Ag-Au NRs. The attachment of DTNB to Ag-Au NRs did not result in a notable shift in the UV–Vis spectral wavelength, and there was a decrease in absorbance. However, SERS characterization, as shown in Fig. 3(a), confirmed the successful attachment of DTNB. Further, the immobilization of ChOx resulted in ~11 nm wavelength shift in the UV–Vis spectrum of DTNB-Ag-Au NRs. Similarly, Fig. 4(b) (ii) shows the attachment of 4ATP and Lp on Ag-Au NRs. The UV–Vis spectrum of Ag-Au NRs showed a concurrent wavelength shift of ~7 nm and ~2 nm with subsequent attachment of 4ATP and Lp, respectively. The reason for such observations could be

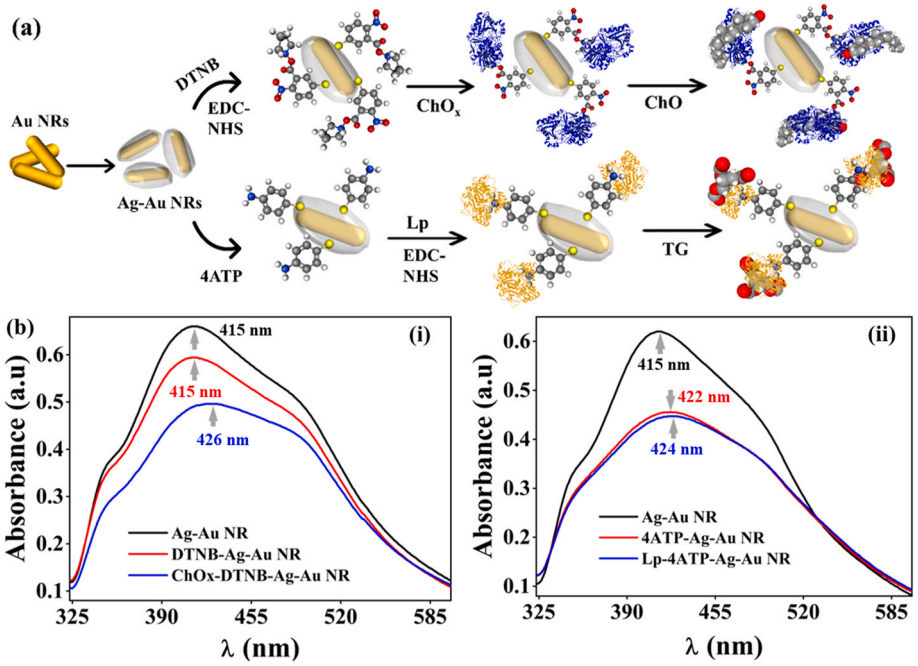

Fig. 4. (a) Schematic showing the immobilization of ChOx and Lp on DTNB–Ag–Au NRs and 4ATP–Ag–Au NRs and (b) UV–Vis spectroscopic characterization of the immobilization of (i) ChOx and (ii) Lp on Ag–Au NRs.

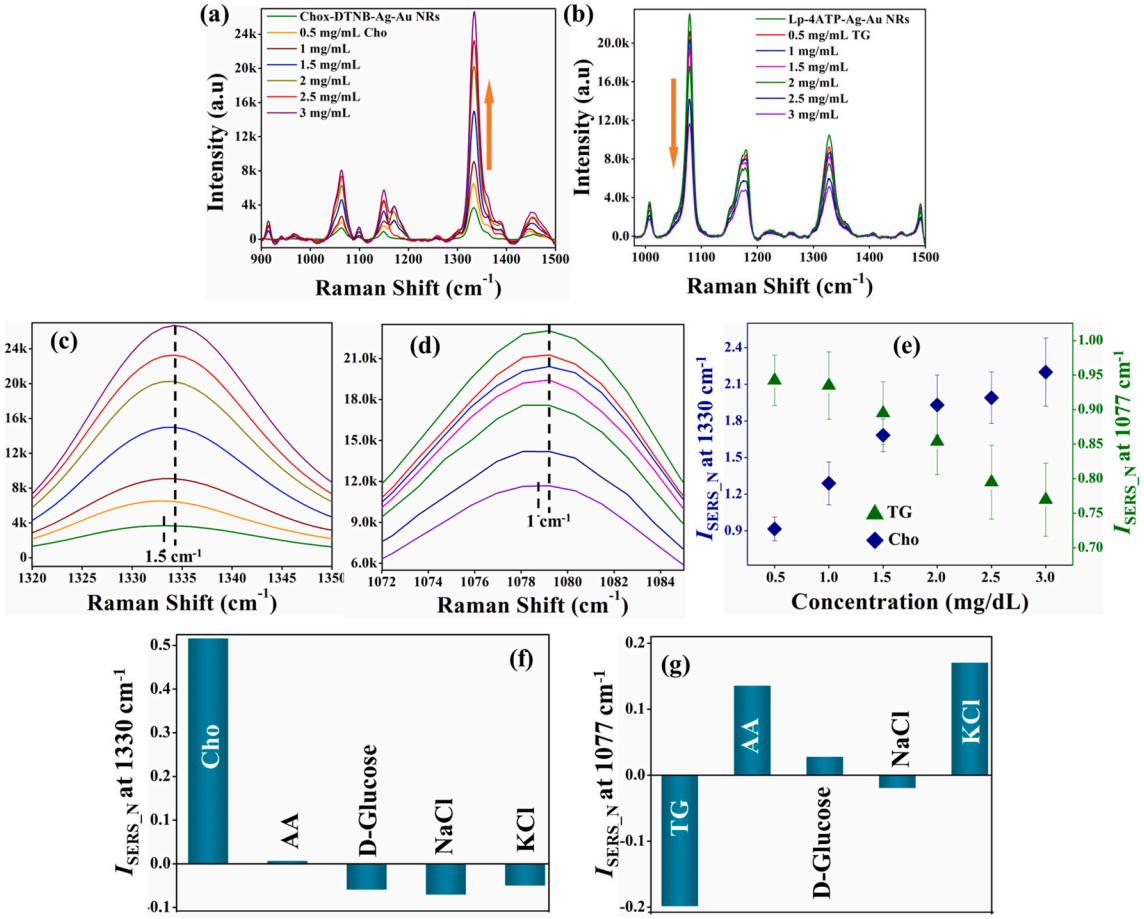

Fig. 5. Shows change in SERS intensity of (a) ChOx–DTNB–Ag–Au NRs and (b) Lp–4ATP–Ag–Au NRs with different concentrations of Cho and TG, respectively. The figure shows the shift in the wavenumber after the reaction of (c) Cho with ChOx–DTNB–Ag–Au NRs and (d) TG with Lp–4ATP–Ag–Au NRs (e) shows the calibration plot for the detection of Cho and TG, (f) validation study for Cho with ChOx–DTNB–Ag–Au NRs and (g) Lp with Lp–4ATP–Ag–Au NRs.

attributed to the change in the local refractive index surrounding the Ag–Au NRs after the immobilization of the enzymes which shifted the LSPR spectrum of the Ag–Au NRs to the longer wavelength (Basak et al., 2021b; Nirala et al., 2018), and thus confirming their attachment to the surface. Further, the immobilization of ChOx and Lp was also confirmed using FTIR analysis as shown in Section S4 of the ESI.

For the detection of Cho and TGl, SERS analysis was employed to observe the interaction of different concentrations of Cho and Glycerol Trioleate (TG) with ChOx–DTNB–Ag–Au NRs and Lp–4ATP–Ag–Au NRs, respectively. As per clinical reports (Children and Pediatrics, 1992), the desirable level of total Cho in blood should be less than 2 mg/mL for adults and 1.7 mg/mL for children. An elevated level exceeding 2.4 mg/mL is considered alarming. For TGl (Caudill et al., 1998), the desirable level is 1.5 mg/mL for adults and 0.9 mg/mL for children. TGl level higher than 2 mg/mL, is a case of hypertriglyceridemia. Therefore, considering the clinical range of Cho and TGl, different concentrations of Cho and TG were prepared – 0.5 mg/mL, 1 mg/mL, 1.5 mg/mL, 2 mg/mL, 2.5 mg/mL, and 3 mg/mL, following the protocol stated in ESI.

For the reaction of Cho (or TG) with ChOx–DTNB–Ag–Au NRs (or Lp–4ATP–Ag–Au NRs), 25 μL of different concentrations of ChO (or TG) were added to six different glass vials containing 1 mL of ChOx–DTNB–Ag–Au NRs (or Lp–4ATP–Ag–Au NRs) and was incubated in a water bath maintained at ~ 40 °C for ~ 30 min. After the reaction, the solutions were allowed to cool to room temperature before the SERS examinations were performed. For the SERS study of total Cho (or TG), at first, 800 μL of ChOx–DTNB–Ag–Au NRs (or Lp–4ATP–Ag–Au NRs) was taken in a cuvette and SERS was performed in liquid mode which marked the baseline for further analysis. After that, 800 μL of different concentrations of Cho–ChOx–DTNB–Ag–Au NRs (or TG–Lp–4ATP–Ag–Au NRs) were analyzed sequentially.

Fig. 5 depicts the SERS analysis performed to characterize the respective enzymatic reactions. Fig. 5(a) shows the change in the SERS spectral intensity for different concentrations of Cho reacting with ChOx–DTNB–Ag–Au NRs. The figure illustrates that the SERS intensity of ChOx–DTNB–Ag–Au NRs increases gradually after reaction with increasing concentrations of Cho with a shift in the Raman band towards higher wavenumber by ~1.5 cm^{-1} as shown in Fig. 5(c). Here, Raman band at 1333 cm^{-1} has been considered for the study owing to pronounced SERS intensity and substantial responsiveness.

Similarly, Fig. 5(b) and (d) show the gradual decrease in SERS spectral intensity of Lp–4ATP–Ag–Au NRs on reacting with increasing concentrations of TG with a shift of Raman band at 1077 cm^{-1} by ~ 1 cm^{-1} towards the higher wavenumber. The reason for such concentration induced frequency shift could be attributed to the bonding of Cho to ChOx–DTNB–Ag–Au NRs or TG to Lp–4AT–Ag–Au NRs, respectively. The formation of enzyme substrate complex induces a stress due to conjunction and creates a tension load on the adsorbed DTNB or 4ATP causing tensile deformation of the corresponding bands. Also, the bonding of Cho to ChOx and TG to Lp promotes an alteration of the electron cloud distribution causing a change in the polarizability of the DTNB–Ag–Au NR and Lp–Ag–Au NR system. This persuades a simultaneous effect on the charge transfer from Ag–Au NR to DTNB/4ATP, which may be a probable reason for the variation in SERS intensities and shift in Raman bands for the two cases (Ma et al., 2019). Additionally, when Cho is allowed to interact with ChOx-DTNB-Ag-Au NRs, the reaction of Cho with ChOx produces hydrogen peroxide and cholest-4-en-3-one. The generated hydrogen peroxide induces the controlled aggregation of the colloidal nanostructures, as observed in the samples after reaction, causing increase in the LSPR hotspots, which is reported to be the reason for the enhanced SERS signals of the DTNB spectral peaks (Gorbachevskii et al., 2018). In contrast, in case of reaction of TG with Lp-4ATP-Ag-Au NRs, it produces glycerol and fatty acids. The adsorption of glycerol and fatty acids thus generated creates a coating over the nanostructure surface causing a shielding of the light interaction with 4ATP molecules, which can be hypothesized as one of the reasons for the decrease in the SERS spectral intensity of 4ATP (Díaz-Amaya et al., 2019).

Fig. 5(e) shows the calibration graph for the measurement of different concentrations of Cho and TG. The graph was prepared by plotting the normalized SERS intensity (I_{SERS_N}) of Cho–-ChOx–DTNB–Ag–Au NRs to ChOx–DTNB–Ag–Au NRs at 1333 cm^{-1} and TG–Lp–4ATP–Ag–Au NRs to Lp–4ATP–Ag–Au NRs at 1077 cm^{-1} for different concentrations of Cho and TG, respectively. The plot shows a good linear trend in the variation of SERS intensities with different concentrations of Cho and TG. Tables S2 and S3 in ESI lists the comparison of LOD and sensitivity of Cho and TG detection in the present work with previous reports.

Further, an interference study was performed to validate the specificity of the proposed sensing technique. For the validation study, the four major interfering agents present in blood were employed: viz ascorbic acid (AA), D–Glucose (D–Glu), sodium ion (NaCl), and potassium ion (KCl). The experimental procedure for testing the effect of the listed interfering agents was similar to as used for testing different concentrations of Cho and TG as discussed in the ESI.

At first, SERS spectra of the enzyme immobilized nanostructures were obtained and marked as baseline. Thereafter, the SERS spectra for Cho, AA, D–Glu, NaCl, and KCl reacted with ChOx–DTNB–Ag–Au NRs were obtained, individually. For validation study of Lp–4ATP–Ag–Au NRs, similar experiments were repeated with 2 mg/mL of TG instead of 2 mg/mL of Cho, else remains same. The change in the SERS intensity of ChOx–DTNB–Ag–Au NRs and Lp–4ATP–Ag–Au NRs before and after the reaction was normalized to prepare the validation plots, as shown in Fig. 5(f) and (g). Fig. 5(f) illustrates that only in the presence of Cho, the normalized SERS intensity (I_{SERS_N}) increases, similar to as obtained in Fig. 5(a). For all other cases, either no change or an opposite trend was observed. Similarly, the plots in Fig. 5(g) show a decrease in normalized SERS intensity only for TG, similar to Fig. 5(b) unlike other interfering agents showing minimal or opposite trend in change in SERS intensity. Therefore, the plots in Fig. 5 demonstrates that the SERS based detection of Cho and TG has the potential to serve as a pivotal technique for multiplexed identification of lipid profile.

4. Conclusions

In summary, the study focuses on the development of a sensing technique utilizing SERS of plasmonic bimetallic nanostructures. Herein, the synthesized bimetallic nanostructures, Ag–Au NRs exhibit enhanced LSPR characteristic as compared to pristine silver and gold nanostructures owing to plasmonic spectral hybridization. These nanostructures demonstrate ~20-fold and more than ~50-fold enhancement in the SERS spectral peaks of DTNB and 4ATP, respectively, as compared to its gold nanorods counterparts. Further, the enriched SERS characteristics of Ag–Au NRs were employed for the detection of ChO and TGl by immobilizing ChOx and Lp linked to the SERS active molecules to form ChOx-DTNB–Ag–Au NRs and Lp-4ATP–Ag–Au NRs. These enzyme–modified nanostructures were then utilized to observe the variation in SERS spectral peaks of DTNB and 4ATP on interaction with different concentrations of ChO and TG, respectively. Interference study with ascorbic acid, glucose, sodium, and potassium ion showed the selectivity and specificity of the sensor.

CRediT authorship contribution statement

Mitali Basak: Writing – review & editing, Writing – original draft, Validation, Methodology, Investigation, Formal analysis, Data curation, Conceptualization. **Harshal B. Nemade:** Writing – review & editing, Validation, Supervision, Formal analysis. **Dipankar Bandyopadhyay:** Writing – review & editing, Validation, Supervision, Resources, Project administration, Funding acquisition, Formal analysis, Conceptualization.

Declaration of competing interest

The authors declare no conflict of interest regarding the submitted article.

Acknowledgments

We thank the Government of India for providing financial support through MeitY Grant no. 5(1)/2022–NANO and ICMR Grant no. 5/3/8/20/2019–ITR.

Appendix A. Supplementary data

Supplementary data to this article can be found online at https://doi.org/10.1016/j.bios.2024.116885.

Data availability

Data will be made available on request.

References

Amiri, M., Arshi, S.J.E., 2020. Electroanalysis 32 (7), 1391–1407.
Anderson, W.E., Williams, H.H., 1937. Physiol. Rev. 17 (3), 335–372.
Basak, M., Mitra, S., Agnihotri, S.K., Jain, A., Vyas, A., Bhatt, M.L.B., Sachan, R., Sachdev, M., Nemade, H.B., Bandyopadhyay, D., 2021. ACS Appl. Bio Mater. 4 (6), 5378–5390.
Basak, M., Mitra, S., Gogoi, M., Sinha, S., Nemade, H.B., Bandyopadhyay, D., 2022. ACS Appl. Bio Mater. 5 (11), 5321–5332.
Caudill, S.P., Smith, S.J., Cooper, G.R., Myers, G.L., 1998. Clin. Chem. 44 (5), 1063–1066.
Children, N., Pediatrics, A.J., 1992. National Cholesterol Education Program (NCEP): highlights of the report of the expert panel on blood cholesterol levels in children and adolescents 89 (3), 495–501.
Díaz-Amaya, S., Lin, L.-K., Deering, A.J., Stanciu, L.A., 2019. Anal. Chim. Acta 1081, 146–156.
Gabudean, A., Biro, D., Astilean, S., 2011. J. Mol. Struct. 993 (1–3), 420–424.
Giannini, V., Fernández-Domínguez, A.I., Sonnefraud, Y., Roschuk, T., Fernández-García, R., Maier, S.A., 2010. Small 6 (22), 2498–2507.
Gorbachevskii, M., Kopitsyn, D., Kotelev, M., Ivanov, E., Vinokurov, V., Novikov, A., 2018. RSC Adv. 8 (34), 19051–19057.
Haes, A.J., Zou, S., Schatz, G.C., Van Duyne, R.P., 2004. J. Phys. Chem. B 108 (22), 6961–6968.
Hooda, V., Gahlaut, A., Gothwal, A., Hooda, V., 2018. Artif. Cells, Nanomed. Biotechnol. 46 (Suppl. 2), 626–635.
Jia, K., Khaywah, M.Y., Li, Y., Bijeon, J.L., Adam, P.M., Déturche, R.g., Guelorget, B., François, M., Louarn, G., Ionescu, R.E., 2014. ACS Appl. Mater. Interfaces 6 (1), 219–227.
Johnson, E.J., Mohn, E.S., 2015. Fat-soluble vitamins. Nutrition for the Primary Care Provider. Karger Publishers, pp. 38–44.
Kritchevsky, D., 1995. JNB (J. Nutr. Biochem.) 6 (4), 172–178.
Lawes, C.M., Vander Hoorn, S., Law, M.R., Rodgers, A., 2004. High blood pressure. Comparative Quantification of Health Risks: Global and Regional Burden of Disease Attributable to Selected Major Risk Factors. World Health Organization, Geneva, pp. 281–390.
Lawrence, G.D., 2010. The Fats of Life: Essential Fatty Acids in Health and Disease. Rutgers University Press.
Ma, H., Liu, S., Zheng, N., Liu, Y., Han, X.X., He, C., Lu, H., Zhao, B.J.A.c., 2019. Anal. Chem. 91 (15), 9376–9381.
Mellanby, E., 1933. Edinb. Med. J. 40 (4), 197.
Mitra, S., Basak, M., 2022. Mater. Today 57, 225–261.
Mondal, K., Ali, M.A., Singh, C., Sumana, G., Malhotra, B.D., Sharma, A., 2017. Sensor. Actuator. B Chem. 246, 202–214.
Morris, A.L., Mohiuddin, S.S., 2020. Biochemistry, nutrients.
Nirala, N.R., Saxena, P.S., Srivastava, A., 2018. Spectrochim. Acta 190, 506–512.
Nordestgaard, B.G., Varbo, A.J., 2014. Lancet 384 (9943), 626–635.
Nordestgaard, B.G., 2017. JACC (J. Am. Coll. Cardiol.) 70 (13), 1637–1646.
Norum, K.R., Berg, T., Helgerud, P., Drevon, C.A., 1983. Physiol. Rev. 63 (4), 1343–1419.
Rhee, K., Tukova, A., Yaraki, M.T., Wang, Y.J.N., 2023. Nanoscale 15 (5), 2087–2095.
Soppert, J., Lehrke, M., Marx, N., Jankowski, J., Noels, H., 2020. Adv. Drug Deliv. Rev. 159, 4–33.
Stein, E., Myers, G., 1995. Clin. Chem. 41 (10), 1421–1426.
Sun, D., Cao, F., Tian, Y., Li, A., Xu, W., Chen, Q., Shi, W., Xu, S., 2019. Anal. Chem. 91 (24), 15484–15490.
Tahir, M.A., Dina, N.E., Cheng, H., Valev, V.K., Zhang, L., 2021. Nanoscale 13 (27), 11593–11634.
Trajkovska, K.T., Topuzovska, S., 2017. Anatol. J. Cardiol. 18 (2), 149.
Wakil, S.J., Abu-Elheiga, L.A., 2009. JLR (J. Lipid Res.) 50, S138–S143.
Yang, D., Wang, J., Cao, Y., Tong, X., Hua, T., Qin, R., Shao, Y., 2023. ACS Appl. Electron. Mater. 5 (2), 593–611.
Zhang, Y., Zhao, S., Zheng, J., He, L., 2017. TrAC, Trends Anal. Chem. 90, 1–13.
Zhu, J., Zhao, B.-z., Qi, Y., Li, J.-J., Li, X., Zhao, J.-W., 2018. Sensor. Actuator. B Chem. 255, 2927–2935.